Research Article

Lithography-Free, Large-Area Spatially Segmented Disordered Structure for Light Harvesting in Photovoltaic Modules

Joo Hwan Ko, So Hee Kim, Min Seok Kim, Se-Yeon Heo, Young Jin Yoo, Yeong Jae Kim, Heon Lee, and Young Min Song*

Read Online

ACCESS | Metrics & More | Article Recommendations | Supporting Information

ABSTRACT: Optical losses in photovoltaic (PV) systems cause nonradiative recombination or incomplete absorption of incident light, hindering the attainment of high energy conversion efficiency. The surface of the PV cells is encapsulated to not only protect the cell but also control the transmission properties of the incident light to promote maximum conversion. Despite many advances in elaborately designed photonic structures for light harvesting, the complicated process and sophisticated patterning highly diminish the cost-effectiveness and further limit the mass production on a large scale. Here, we propose a robust/comprehensive strategy based on the hybrid disordered photonic structure, implementing multifaceted light harvesting with an affordable/scalable fabrication method. The spatially segmented structures include (i) nanostructures in the active area for antireflection and (ii) microstructures in the inactive edge area for redirecting the incident light into the active area. A lithography-free hybrid disordered structure fabricated by the thermal dewetting method is a facile approach to create a large-area photonic structure with hyperuniformity over the entire area. Based on the experimentally realized nano-/microstructures, we designed a computational model and performed an analytical calculation to confirm the light behavior and performance enhancement. Particularly, the suggested structure is manufactured by the elastomeric stamps method, which is affordable and profitable for mass production. The produced hybrid structure integrated with the multijunction solar cell presented an improved efficiency from 28.0 to 29.6% by 1.06 times.

KEYWORDS: light harvesting, disordered structure, antireflection, encapsulation layer, photovoltaic, solar cell
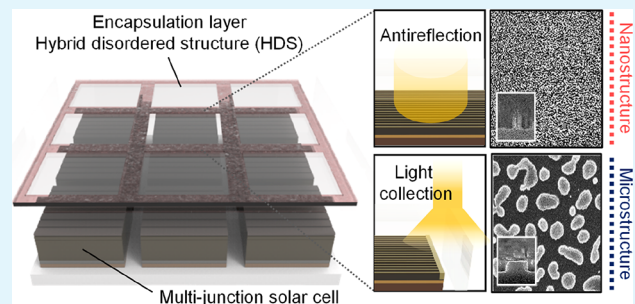
INTRODUCTION

The ever-increasing advances of the photovoltaic (PV) industry facilitate the utilization of solar light as a next-generation energy source due to its sustainability and renewability. Over the past years, as the installed PV capacity is doubling, the cost of PV panels (per power generation, PG) has continuously decreased by 40%.[1] In the streamlined research, several technical improvement methods have been suggested to achieve highly affordable and efficient solar energy conversion. A significant factor to reduce the installation costs of PV (per PG) is to increase the energy conversion efficiency of the solar cells itself.[2] For all PV systems, optical loss is a major factor that hinders the attainment of the Shockley–Queisser limit: (1) a certain amount of sunlight is reflected off the cell surface, (2) absorbed by the inactive layer of the PV module, or (3) incompletely trapped inside the semiconductor.[3] All these phenomena reduce the photocurrent that can be achieved in cells.[4−6] To overcome the limitations, a strategy to reduce the inactive area of the solar cell and efficient light delivery to the active area is highly required, eliminating losses from nonradiative recombination or incomplete absorption.[7,8] The incorporation of properly

designed nanostructures to control the flow of light reduces the aforementioned optical losses and mitigates optical absorption, increasing the photocurrent, particularly through encapsulation layers.[9−11] Encapsulation is the final step in the modularization of solar cells, and it covers the surface of the cell and controls the transmission properties of the incident light to promote maximum conversion in the primary cell without affecting its intrinsic behavior.[12] Based on the design of the photonic structure to deliver sunlight into the active area, structural approaches such as the use of prisms,[13] randomly scattered pyramid structures,[14,15] tapered structures,[16,17] diffraction gratings,[18,19] correlating nanostructure,[20] and periodic/nonperiodic array[21,22] have been reported. Fundamentally, focused on either antireflection (AR) or light redirection, its designing and processing results are successfully
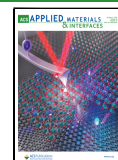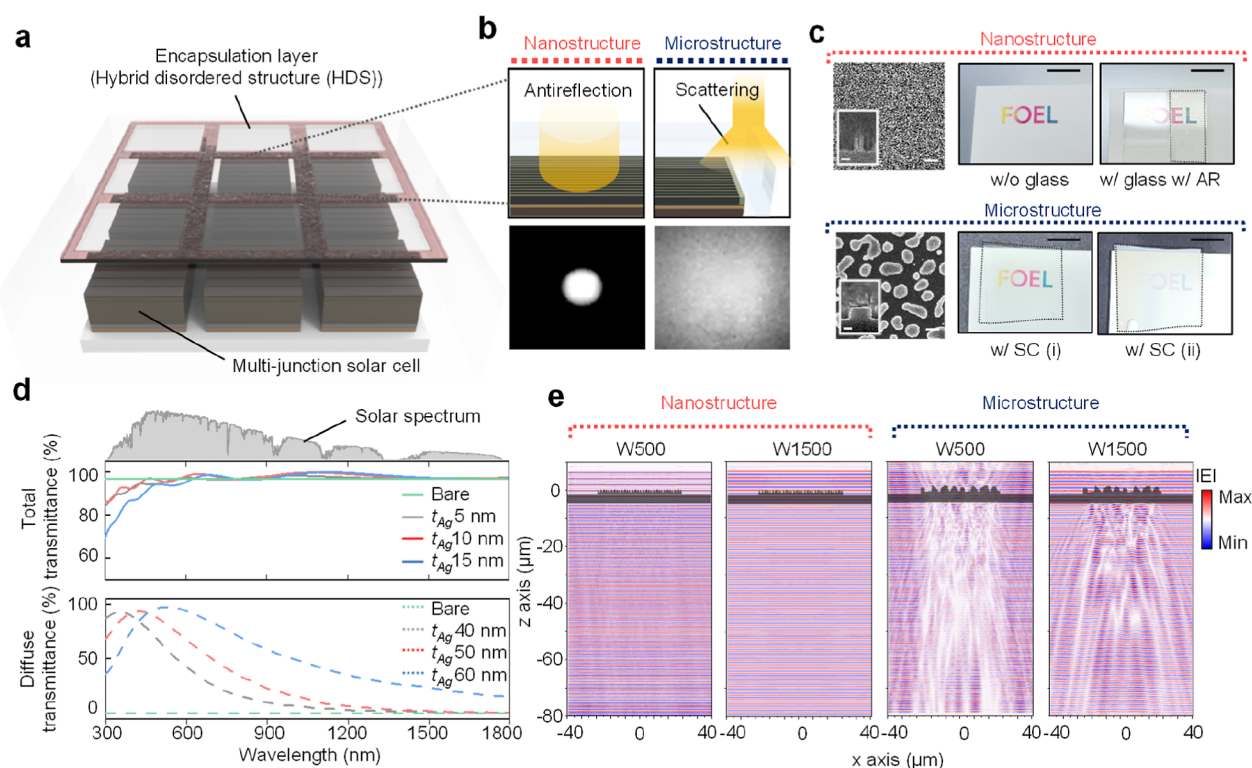
Figure 1. (a) Schematic of an encapsulation layer with HDS integrated on a MJSC. (b) Schematic views and photographs of two types of disordered structures (*i.e.*, nano-/microstructures) with a collimated light source. (c) SEM image of the optimized nano-/microstructure at top view and cross-sectional view (left). Scale bar is 500 nm. Photographs of AR and scattering (SC) structure. SC (i) and (ii) refer to the vertical distance of 0 and 5 mm, respectively (*i.e.*, the distance represents the gap between printed paper and SC-PDMS). Scale bar is 1 cm. (d) Calculated specular transmittance of AR-PDMS for t_{Ag} = 5, 10, and 15 nm (top) and diffuse transmittance spectra for t_{Ag} = 40, 50, and 60 nm (bottom). (e) Calculated electric field distribution of SC-PDMS according to the nanostructure (*i.e.*, t_{Ag} 10 nm) and microstructure (*i.e.*, t_{Ag} 60 nm) at wavelengths of 500 and 1500 nm.

presented.[23−25] However, to address the entailing issues from optical losses,[3] a more robust/comprehensive strategy is necessary, which can simultaneously control the incident light to achieve AR,[26] light collection,[27] and complete light trapping.[28,29] Furthermore, to maximize the light harvesting performance with satisfactory cost-effectiveness of modularization of the PV system and scalability, simple-processed and affordable photonic structures are required. However, the complicated process and the sophisticated pattering still highly diminish the cost-effectiveness and further limit the mass production on a large scale.[30−33]

Here, we present a hybrid photonic encapsulation layer based on scalable and lithography-free nano-/microstructures as a simple and facile approach to simultaneously control the sunlight, enabling AR and light capturing. Even with an ultrathin and lightweight configuration, the encapsulation layer efficiently collects the unused light into the cell area and significantly reduces surface reflection, thereby enhancing the photocurrent and conversion efficiency. A lithography-free hybrid disordered structure (HDS) is fabricated by the thermal dewetting method to construct a large-area photonic structure with uniform metal nanoparticles over the entire area.[34−37] The degree of disorder, the size of the nano-/microrod, and thickness are elaborately controlled. For numerical confirmation, we suggest a computational model based on a real fabricated structure, considering its configuration and scale for optical calculation. In the process, rigorous coupled-wave analysis (RCWA) is performed by sweeping the dimension of the structure and the wavelength of incident light. From the

results, we optimized the best structures by characterizing the transmittance, absorption of cell, and interaction between electric field and structures. Furthermore, the suggested photonic structure is manufactured by the elastomeric stamps method,[38] which is repeatedly replicable and transferable, thus resulting in an affordable manufacturing cost. Empowered by the suggested design flows, the fabricated structure facilitates the realization of a high-performance, scalable, and cost-effective light harvesting platform.

■ RESULTS AND DISCUSSION

Encapsulation Layer and Light Harvesting. Figure 1a shows a schematic of the encapsulation layer according to the proposed strategy to enhance the optical energy collection integrated on the multijunction solar cells (MJSCs). The layer comprises a HDS, which is divided into two types of area: (1) nanostructure and (2) microstructure. The behavior of the light passing through HDS is briefly represented in Figure 1b by irradiating a collimated light beam (SLS400, Thorlabs, Inc., Germany) into nano-/microstructures. Each part is placed on the active cell area and inactive edge area as a function of AR to reduce surface reflection and scattering (SC) for light delivery into the cell area. In this step, we fabricated different-sized random structures with the nano-/microscale by controlling the thickness of the metal (Ag) layer (see the Experimental Section for the detailed process). As presented in Figure 1c, the fabricated random nanostructure, that is, AR layer, shows a subwavelength structure with a disordered pattern, with a clear image without surface reflection.
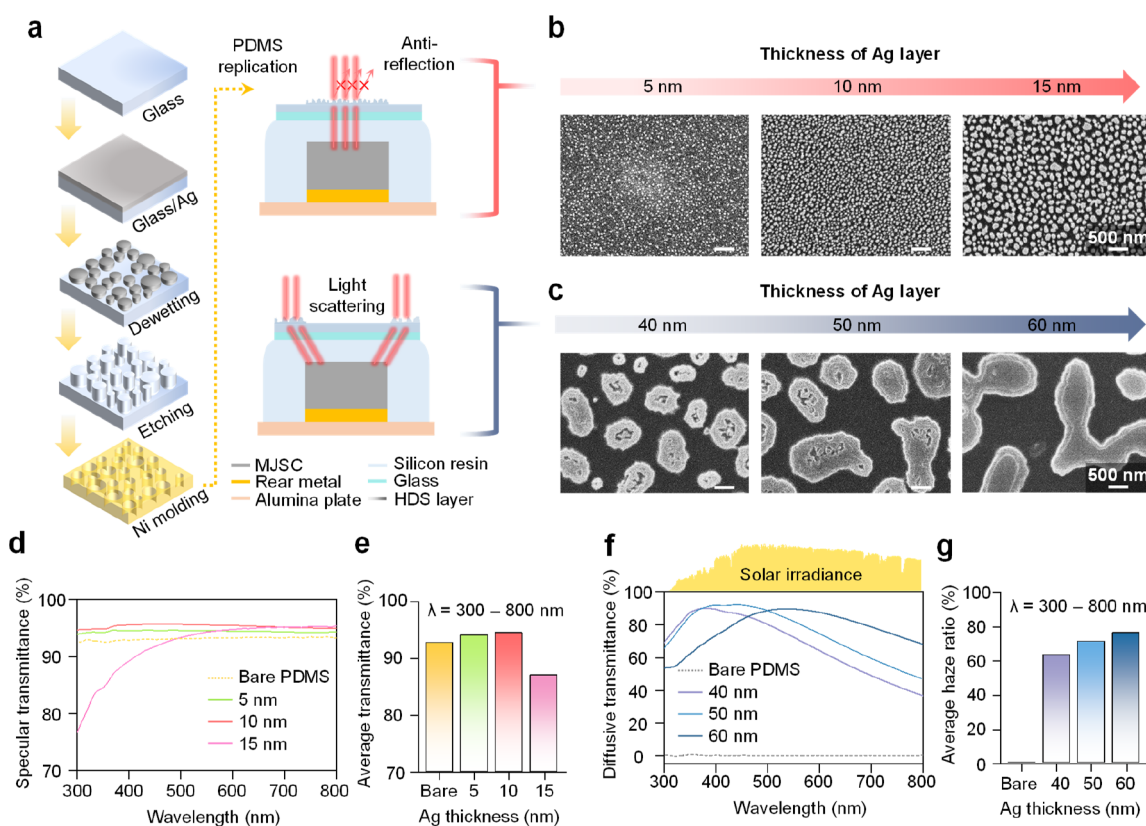
Figure 2. (a) Schematic of the fabrication process of the HDS with PDMS (left) and different optical functions of the disordered structure (right). (b) SEM images of the AR structure (*i.e.*, t_{Ag} = 5, 10, and 15 nm). (c) SEM images of the scattering structure (*i.e.*, t_{Ag} = 40, 50, and 60 nm). (d) Measured specular transmittance of the AR structure. (e) Averaged transmittance of (d). (f) Solar irradiance spectrum and measured diffusive transmittance of the scattering structure. (g) Averaged haze ratio derived from (f).

Contrarily, the scanning electron microscopy (SEM) image of the random microstructure, that is, the SC layer, represents a relatively large-scale rod shape than the wavelength regime with a hazed optical microscope image. To understand the light−matter interaction between sunlight and HDS, we conceived structural modeling and optical simulation. From the realized sample, we extracted geometrical information (*i.e.*, distribution and rod shape) obtained from SEM images for numerical analysis. In the computational model, we set the height (h) of the AR/SC structure as 400 nm/800 nm (see Figure S1, Supporting Information). Using the addressed analytical model, we calculated the transmittance passing through each structure (Figure 1d). Among the zeroth-order transmittance of the AR structures, 10 nm of Ag thickness (t_{Ag}) shows the highest average transmission of 97.0% in the wavelength region of 300−1800 nm. To enable a highly antireflective condition, a gradient refractive index and an effective medium without higher order diffraction should be satisfied.[39−41] With the increase of t_{Ag}, the rod size is widened, producing higher diffraction order (see Figure S2, Supporting Information). The transmission characteristics were also expressed by solar weighted transmittance (SWT), which is the ratio of usable photons to the total transmitted photons. The SWT is evaluated by normalizing the transmittance spectra with the solar spectral photon flux (*i.e.*, AM 1.5 G) integrated over a wavelength range,[42] and eq 1 is given by

$$\text{SWT} = \frac{\int I_s(\lambda)T(\lambda)\mathrm{d}\lambda}{\int I_s(\lambda)\mathrm{d}\lambda} \qquad (1)$$

where $I_s(\lambda)$ is the spectral irradiance (in this study, we used AM 1.5 G) and $T(\lambda)$ is the total transmittance. As expected, the SWT of t_{Ag} 10 nm shows the highest value (97.05%), which is extracted from the specular transmittance spectra in Figure 1d (see Table S1, Supporting Information). In the case of the scattering medium, to confirm efficient light delivery into the cell area, diffusive transmittance was considered. With t_{Ag} 40, 50, and 60 nm, the optical simulation results based on the analytic model show that the transmission peaks are placed at the wavelengths of 350, 420, and 520 nm, respectively. We note that the peak position of diffusive transmittance of t_{Ag} 60 nm closely corresponds to the highest solar intensity in the solar spectrum (near λ = 550 nm). Likewise, the SWT of t_{Ag} 60 nm shows the highest value (70.03%) from the diffusive transmittance in Figure 1d (see Table S1, Supporting Information). Comprehensively, we selected the best conditions for HDS (t_{Ag} 10 nm and 60 nm for AR and SC, respectively). Furthermore, the electric field (e-field) distributions were calculated at the wavelengths of 500 and 1500 nm, respectively. The used computational model is extracted from the geometrical shape/distribution from the fabricated samples (*i.e.*, for nanostructure, t_{Ag} 10 nm/h 400 nm, and for microstructure, t_{Ag} 60 nm/h 800 nm) (see Figure S1, Supporting Information). As a result, with the AR structure, the plane wave of incident light passes through the layer without any other diffraction. However, the e-field passing through the SC structure is partially redirected and diffused at the microstructure from the normally incident light on the surface.
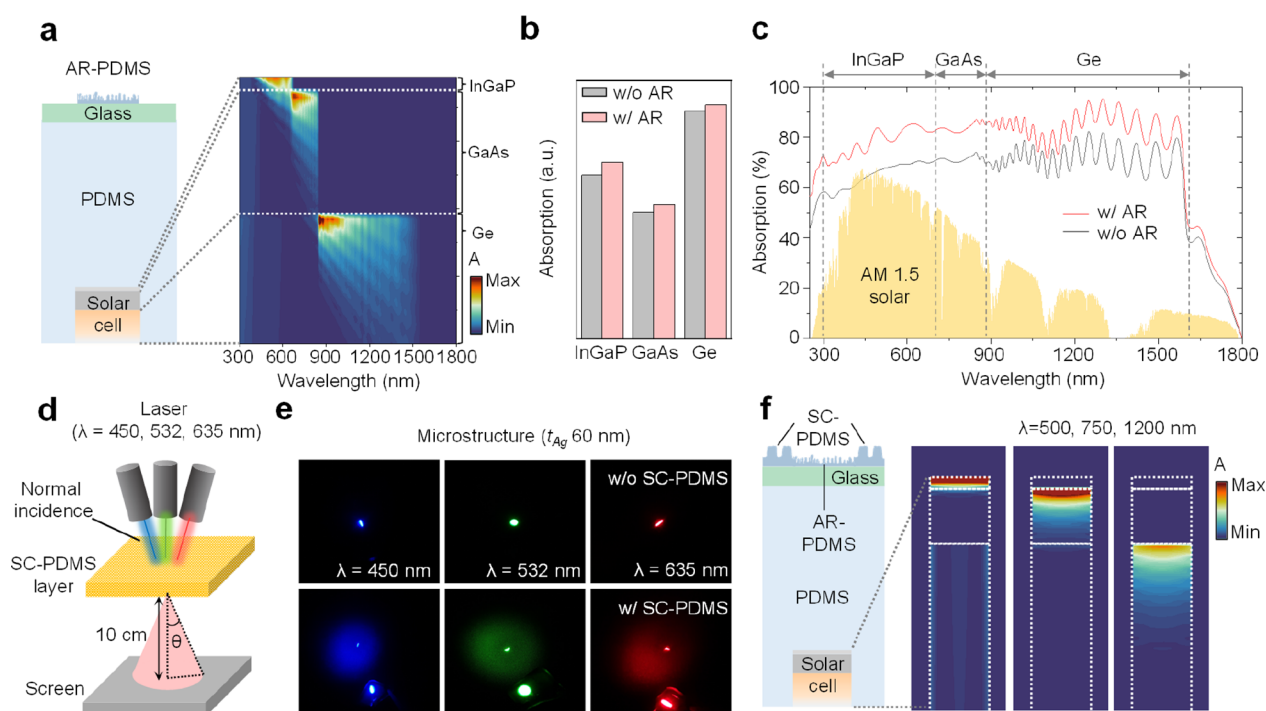
Figure 3. (a) Simulated absorption profiles of the MJSC combined with AR-PDMS for three different active layers (*i.e.*, InGaP, GaAs, and Ge) with the spectrum range from 300 to 1800 nm. (b) Calculated absorptance and comparison of the integrated absorption intensity in three active layers (*i.e.*, $In_{0.5}Ga_{0.5}P$, GaAs, and Ge) by applying the AR-PDMS layer. (c) Calculated absorption spectra of the AR-PDMS layer on a solar cell with the solar irradiance spectrum. (d) Schematic of the measurement setup for SC-PDMS using laser beams (λ = 450, 532, and 635 nm). (e) Photographs of three diffused areas with wavelengths of 450, 532, and 635 nm. (f) Schematic of the MJSC with the HDS-PDMS layer (left). Calculated absorption profiles of the MJSC combined with the HDS-PDMS layer for three wavelengths (*i.e.*, 500, 750, and 1200 nm).

Manufacturing and Structural Optimization of HDS.

As a replication medium, we selected polydimethylsiloxane (PDMS) as a medium material for fabricating HDS due to its affordable (*i.e.*, reproducible) and efficient (*i.e.*, low surface reflection for AR) properties. To realize a hybrid structure with nano-/microdimensions, we first fabricated the spatially segmented rods divided into the AR and SC region. Then, the Ni stamp was fabricated as a replication mold. Finally, the PDMS was cured and detached (see the Experimental Section and Figure S2, Supporting Information). Figure 2a (left) shows the brief schematic of the fabrication process of the HDS-PDMS layer from structure formation to PDMS replication. As the Ni mold is fabricated with a reverse shape from the nano-/ microstructure of glass, the replicated PDMS has the same shape as the original structures. As depicted in Figure 2a (right), each part of HDS represents a different function. Therefore, to characterize the physical/optical property, we fabricated the AR (t_{Ag} = 5, 10, and 15 nm) and SC structures (t_{Ag} = 40, 50, and 60 nm), respectively. From the realized sample, we conducted structural analysis and optical measurements. First, structural analysis was performed with the SEM image to examine the surface morphology of the nano/ microstructures achieved from the glass substrate. Figure 2b presents the nanostructures, representing the diameter information with different sizes of t_{Ag}. The measured average diameters of the nanostructures (for t_{Ag} = 5, 10, and 15 nm) are 44 ± 12, 68 ± 25, and 130 ± 47 nm, respectively (see Figure S3, Supporting Information). For a PDMS medium (refractive index, $n \sim$ 1.43), a grating period below 200 nm is necessary to remove the higher order diffraction.[39,43] Therefore, in the case of t_{Ag} 15 nm, an additional diffraction order is

generated, causing reduction of specular transmittance (see Figure S4, Supporting Information). Among the various mechanisms of AR, our suggested structure follows the antireflective structure with having the gradient refractive index (see Figure S5, Supporting Information).[44,45] For the scattering layer, Figure 2c shows microstructures, representing relatively large dimensions. Corresponding to the metal layer (t_{Ag} = 40, 50, and 60 nm), the measured average diameters are 690 ± 313, 1024 ± 371, and 1506 ± 755 nm, respectively (see Figure S3, Supporting Information). This tendency is well matched with the previously reported results (*i.e.*, as t_{Ag} increases, the size of the randomly distributed particles increases).[35] Subsequently, the optical measurement was performed with spectroscopy to confirm the specular and diffusive transmittances to examine the optical property of the nano/microstructures achieved by PDMS replication. Furthermore, to evaluate the influencing factor between structural parameter (*e.g.*, size, height, and distribution of rods) and optical output (*e.g.*, diffusive/specular transmittance), we calculated the transmittance by changing the parameters (see Figure S6, Supporting Information). First, in the case of antireflective structures, the size of the rod significantly influences to the overall transmittance intensity. However, the height of rod is less sensitive.[46] Second, the diffusive structures show the high dependency with respect to both the size and height of the rod. As the size and height of rods increase, the peak of diffusive transmittance was moving toward longer wavelength. As described in the Figure S6, various transmittance spectra show a similar property, which is extracted from a single fabricated sample, because the thermal dewetting process make a uniform distribution of nano-/
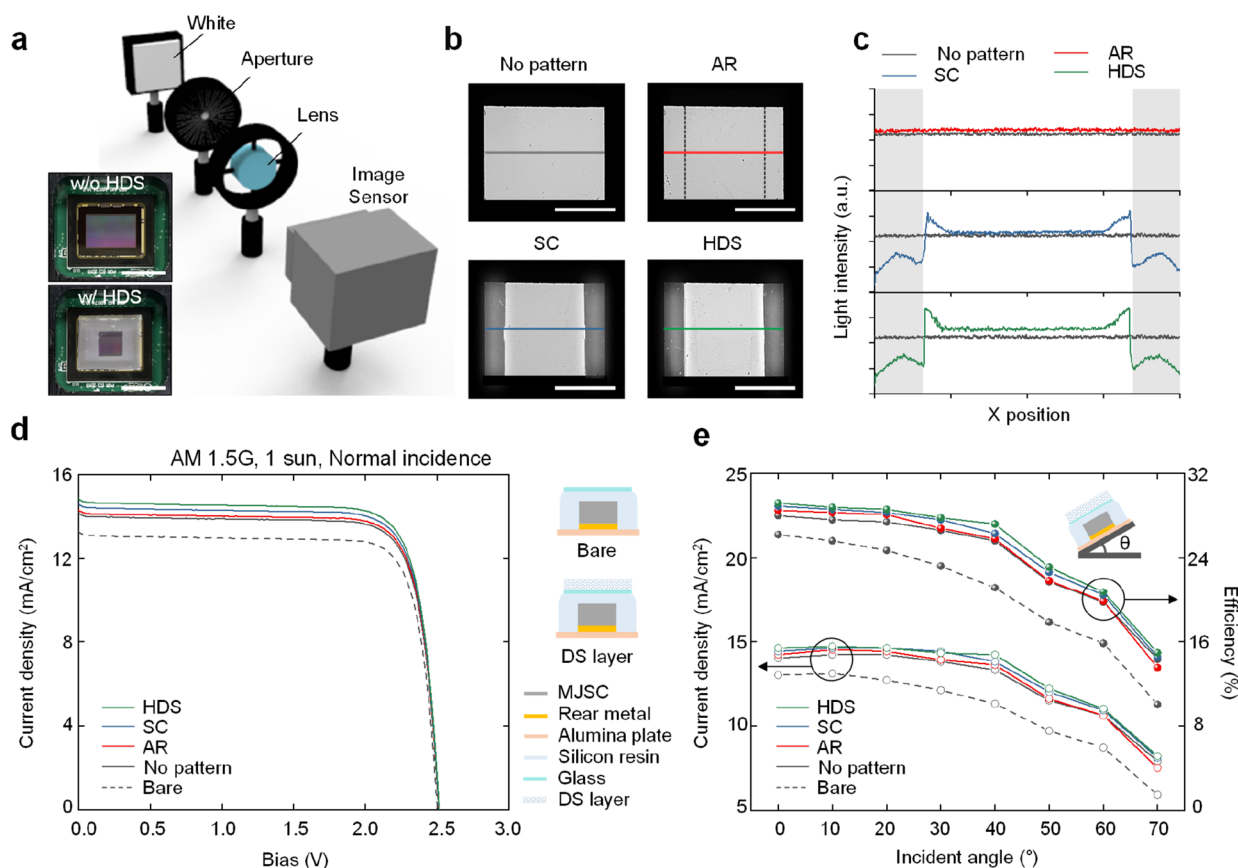
Figure 4. (a) Schematic illustration of the measurement setup for light capturing. Photograph of HDS-PDMS laminated on the cover glass of the CMOS image sensor. Scale bar is 1 cm. (b) Captured photographs with light intensity distribution for different structures (*i.e.*, bare PDMS, AR-PDMS in the center area, SC-PDMS in the edge area, and HDS-PDMS). Scale bar is 0.5 cm. (c) Measured light intensity profile corresponding to the types of structure. (d) Measured current density−voltage (*J*−*V*) curves of the MJSC integrated with bare-/AR-/SC-/HDS-PDMS, respectively. (e) Illumination angle dependency according to the measured short-circuit current (J_{SC}) and power conversion efficiency (η).

microparticles. As represented in Figure 2d, each specular transmittance shows different intensities, and among them, the nanostructure achieved with 10 nm of t_{Ag} shows the highest transmittance value. To evaluate the accurate specification of optical properties of nanostructured PDMS, specular transmittance and diffusive transmittance have been considered for the wavelength range from 300 to 800 nm, which has a major influence on SWT (see Figure S7, Supporting Information). The average specular transmission of the bare PDMS over a wide wavelength range of 300−800 nm is considerably increased from 92.7 to 94.4% (Figure 2e). Furthermore, the SWT shows the highest value (95.27%) for t_{Ag} 10 nm, which shows a good agreement with simulated results (see Table S2, Supporting Information). Likewise, we identified the suppressed surface reflection through the optimized nanostructure (*i.e.*, t_{Ag} = 10 nm), and the average reflection of the bare PDMS is reduced from 7.3 to 5.6% (see Figure S7, Supporting Information). As shown in Figure 2f, the diffusive transmittance spectra are represented with peak intensity at the wavelengths (360, 430, and 530 nm) for microstructures (t_{Ag} = 40, 50, and 60 nm). To quantitatively identify the light diffusion for each microstructure, we measured the diffusive transmittance and calculated the optical haze ratio (H) based on eq 2[47,48]

$$H(\%) = \frac{T_d}{T_t} \times 100 \qquad (2)$$

where T_d and T_t are the diffusive transmittance and total transmittances, respectively, and the calculation has been conducted for the wavelength range from 300 to 800 nm (see Figure S8, Supporting Information). As represented in Figure 2g, the scattering structure with a t_{Ag} of 60 nm has a higher average haze ratio of 76.2% than the cases with a t_{Ag} of 40 and 50 nm (*i.e.*, 63.4% and 71.1%). Furthermore, the peak intensity of t_{Ag} 60 nm is placed at the highest intensity range of the solar spectrum, resulting in effective high-powered sunlight delivery into cell area. Furthermore, the SWT shows the highest value (78.84%) for t_{Ag} 60 nm, which shows a good agreement with simulated results (see Table S2, Supporting Information). Considering the characterization results, we selected t_{Ag} 10 and 60 nm as the AR and SC media, respectively.

Optical Calculation and Experimental Characterization of AR-/SC-PDMS. Figure 3a (left) presents the conceptual cross-sectional view of AR-PDMS attached to the MJSC, which is composed of $In_{0.5}Ga_{0.5}P$ (0.7 μm), GaAs (3.65 μm), and Ge (150 μm). Figure 3a (right) shows the absorption profiles corresponding to the broad spectral range (λ = 300−1800 nm) with AR-PDMS. When compared to absorption of flat PDMS, the MJSC shows higher absorption intensity for all active layers (see Figure S9, Supporting Information).

Figure 3b shows that absorption in the three active layers combined with AR-PDMS is relatively high by 1.15 times compared to the bare MJSC. Furthermore, to confirm the antireflective effect corresponding to the wavelength, we

conceived optical calculation by applying the AR-PDMS layer on a solar cell (Figure 3c). In the spectral range indicated as Ge (λ = 900−1600 nm), the spectrum has a fringe pattern. This phenomenon is originated from the interference of light at the transparent layers (i.e., InGaP/GaAs). Since there is no absorption in the top two layers beyond the wavelength of 900 nm, the interference occurred corresponding to the Swanepoel model,[49] which have fluctuation shape with having maxima and minima absorptance. The absorptance spectra were calculated based on the normal incidence of light. From the spatial (i.e., absorption profile) and spectral (i.e., absorptance spectrum) calculation result, we confirmed that the AR-PDMS layer efficiently promotes light harvesting by eliminating unnecessary surface reflection at the encapsulation coating. To measure the quantitative specifications of SC-PDMS, the light scattering presented by SC-PDMS is experimentally demonstrated under three wavelengths of 450, 532, and 635 nm corresponding to blue, green, and red light, respectively (Figure 3d). The distance between the SC-PDMS layer and the screen was fixed at 10 cm, and the angle of the diffused light of wavelengths 450, 532, and 635 nm passing through the SC-PDMS layer is 21.7, 27.7, and 30.0°, respectively (see Figure S10, Supporting Information). Figure S8 illustrates the measurement setup and the calculation method used to derive the diffraction angle. The measurement results indicate that a light with a longer wavelength is dispersed with a larger angle than the light with a shorter wavelength, which helps redirect the light reaching the inactive area to the cell area. From the results, we confirmed that the SC-PDMS layer of t_{Ag} 60 nm spreads the light widely on the screen (Figure 3e). The optical path length along with the wavelength was evaluated using the projected images. From the simulation and experiment results, to confirm the light harvesting effect, we made the computational design of the integrated HDS-PDMS and MJSC. Figure 3f (left) illustrates the conceptually modeled scheme to identify the enhancement of absorptance. As shown in Figure 3f (right), the absorption layers are changed corresponding to the wavelength, and all the layers of the HDS-PDMS on the MJSC present stronger absorptions than those of bare PDMS and AR-PDMS (see Figure S11, Supporting Information with the comparison of integrated absorption intensity).

Experimental Confirmation of Light Harvesting with the MJSC. From the optimized conditions, we experimentally fabricated the hybrid structures, which have separated area, and the dimension was addressed from the scale of cell and edge region. The HDS-PDMS layer was replicated using a soft lithography method from the Ni mold (see the Experimental Section and Figure S2, Supporting Information). Figure 4a represents the configuration of light capturing the measurement setup, which consists of white light source (light-emitting diode), aperture, lens, and image sensor. The aperture acts as a point source and is located at the focal length of the lens to produce collimated light illumination. The HDS-PDMS is laminated on the cover glass of the complementary metal oxide semiconductor (CMOS) imaging sensor (inset; Figure 4a). Figure 4b shows the captured photographs of irradiance distribution for the different structures (i.e., bare PDMS, AR-PDMS in cell area, SC-PDMS in edge area, and HDS-PDMS). In the case of HDS-PDMS layer, the brightness of the cell area indicates the amount of light transmitted into the image sensor plane. For more detailed analysis on the quantitative light intensity according to structures, we compared the pixel intensity in the center position of the captured image. Figure

4c represents the light intensity profile corresponding to the types of the attached PDMS. The white-/gray-colored region indicates the center/edge area. As shown in the profile of the AR-PDMS layer, the intensity is slightly high compared to the no-patterned bare PDMS layer due to the enhanced antireflective effect. Moreover, in the case of SC-PDMS layer, the light intensity sharply increases near the interface between the cell and edge area due to light scattering. The HDS-PDMS layer combined with the AR-PDMS and SC-PDMS has the highest intensity profile at both the interface and cell area. Therefore, by combining the AR effect and light scattering effect, the HDS-PDMS layer efficiently delivers the incident light to the center area. For practical device applications, the fabricated structures (i.e., bare PDMS, AR-PDMS in the center area, SC-PDMS in the edge area, and HDS-PDMS) were employed in the cover glass of the encapsulation MJSC. To characterize the solar cell parameters, Figure 4d shows the measured current density−voltage (J−V) curves of the MJSC integrated with bare-/AR-/SC-/HDS-PDMS, respectively, by using a solar simulator with AM 1.5 G (Oriel Sol3A, USA) and 1 sun illumination (100 mW/cm²) at 25 °C. The measured MJSC parameters are short-circuit current (J_{SC}), open-circuit voltage (V_{OC}), fill factor (FF), and power conversion efficiency (η), which are summarized in Table 1. η was calculated using eq 3

$$\eta = \frac{J_{sc}\ (\text{mA cm}^{-2}) \times V_{oc}\ (\text{V}) \times \text{FF}\ (\%)}{P_{\text{light}}\ (\text{mW cm}^{-2})} \tag{3}$$

Table 1. Averaged Solar Cell Parameters for Five Different Types of MJSCs[a]

device	J_{SC} (mA/cm²)	V_{OC} (V)	FF (%)	η (%)
bare MJSC	14.0 (0)	2.5 (0)	79.68 (0.07)	27.96 (0.05)
bare-PDMS/MJSC	14.2 (0)	2.5 (0)	79.3 (0.12)	28.2 (0.05)
AR-PDMS/MJSC	14.4 (0.04)	2.5 (0)	79.4 (0.05)	28.6 (0.04)
SC-PDMS/MJSC	14.7 (0)	2.5 (0)	79.1 (0.10)	29.1 (0)
HDS-PDMS/MJSC	14.8 (0.05)	2.5 (0)	79.4 (0.01)	29.6 (0.06)

[a]The standard deviations for each parameter are stated in parentheses (see Table S3, Supporting Information).

where P_{light} represents the power density of the incident light. As the measurement is performed using the bare MJSC, we conducted cross-validation to ensure the uncertainty of the bare MJSC (see Figure S12, Supporting Information). In addition, we performed statistical analysis on several types of encapsulation layers with cross-validation (see Table S3, Supporting Information). As a reference, the J_{SC} MJSC encapsulated by flat glass was measured as 14.0 mA/cm². Further, we confirmed that the efficiency (η) of MJSC with flat PDMS was improved by the enhanced J_{SC} (14.2 mA/cm²) owing to the reduced refractive index variation between the outer environment (air, $n \sim 1$) and the PDMS polymer ($n \sim$ 1.43) than glass ($n \sim 1.5$). In particular, the MJSC integrated with the HDS-PDMS layer exhibited a drastic improvement of J_{SC} from 14.0 to 14.8 mA/cm² due to increased cell absorption. From the experimental results, the efficiency is increased by 1.06 times from 28.0 to 29.6%. To analyze the illumination angle dependency of the HDS-PDMS layer on the MJSC, the J−V measurement was performed with varying incident angle (θ) from 0 to 70°. As θ is increased, J_{SC} and η are gradually

decreased (Figure 4e). Because the absorption intensity is decreased with the increase of incident angle,[50] the J_{SC} was reduced due to the lowered absorption intensity in the semiconductor layer, resulting in low exciton generation rate.[51] Consequently, it reduces the total η following eq 3. However, in the case of the configuration with HDS-PDMS, the reduction is less than that of the bare MJSC with incident angle variation due to the enhanced absorption intensity in active area thanks to the optical effect due to the HDS-PDMS (see Figure S13, Supporting Information).

■ CONCLUSIONS

This study presented an effective strategy for designing a hybrid photonic structure, in which randomly dispersed nano-/microstructures promote antireflective and light scattering, respectively. The suggested structure clearly demonstrated the incident light control, enhancing the light trapping at the cell active layers originated at the AR (surface of active area) and light delivery (from the unused area to the active area). The thickness of the Ag layer determines the scale of the randomly dispersed structures, which affects the optical function of the encapsulation layer. For the best light harvesting performance, t_{Ag} 10 nm was selected as an antireflective function due to its subwavelength scale and gradient refractive index. In the case of the scattering medium, t_{Ag} 60 nm showed high diffusive transmittance and light scattering angle. For the theoretical and experimental analysis, an MJSC (In$_{0.5}$Ga$_{0.5}$P/GaAs/Ge) was selected and integrated with the HDS (optimized configuration), presenting an improvement in the solar gain in the active area, resulting in an efficiency increase by 1.06 times (from 27.96 to 29.6%). Particularly, as the suggested scheme can be manufactured by the elastomeric stamps method, which can be repeatedly replicated, it is suitable for mass production. In our manuscript, PDMS had been used as a polymer medium for replication. Although PDMS shows great optical property (i.e., no absorption) and replicability, they are exposed to harsh applications in outdoor environments, which could cause degradation of the polymer. Nowadays, there are many alternative strategies to overcome ultraviolet (UV)/thermal degradation of polymers (e.g., polyurethane/ZnO composite).[52,53] Based on the suggested anti-UV/thermal degradation polymer, as a future work, additional research for robust replication method is needed.

As a result, in this work, the design process for the lithography-free/hybrid photonic structure has been suggested, and based on the customized computational model, the optical behavior has been elaborately evaluated. From the result, we experimentally realized the HDS-PDMS and characterized the enhancement of solar cell efficiency. Furthermore, the possibility of large-area fabrication will promote the utilization diverse range of optoelectronic devices,[54,55] such as light harvesting system, photoelectric sensors, or water splitting system (see Figure S14, Supporting Information).

■ EXPERIMENTAL SECTION

Optical Simulation. The optical spectra and the absorption profiles were obtained using the commercial software (DiffractMOD, RSoft; USA) based on the RCWA method. In all simulation results, the fifth diffraction order and a grid size of 1 nm were set to numerically stabilize and for accurate results. In electrical field simulations, the finite-difference time domain method was used, and perfectly matched layer domains were considered for horizontal/vertical direction. To achieve accurate calculation results, material dispersions and extinction coefficients were considered. The complex refractive indices of the PDMS polymer were obtained from the existing literature,[56] and semiconductors such as Ge, GaAs, and InGaP were achieved from the literature.[57−59]

Optical and Structural Characterization. The specular and diffusive transmittance spectra were characterized by using an ultraviolet−visible−near-infrared spectrometer (Lambda 950, Perki-nElmer, Inc., USA). To measure the light intensity profile passing through HDS, the customized measurement setup was composed of a white light source (MCWHL6, Thorlabs, Inc., Germany) with a collimated lens (SM2F32-B, Thorlabs, Inc., Germany), an aperture, and a CMOS image sensor (Grasshopper G33-U3-23S6C-C, FLIR, USA). Structural analyses were also performed using a scanning electron microscope (JSM-7500F, JEOL, Japan).

Fabrication of HDS Layer. A clean bare glass substrate with acetone, methanol, and deionized (DI) water was prepared. After dividing the active area and edge area with a shadow mask, Ag was deposited to a thickness of 10 and 60 nm on a substrate using an electron beam evaporator (KVE-E2000, Korea Vacuum Tech, Ltd., Korea) under a high vacuum ($\approx$10^{-6} Torr). To fabricate the disordered Ag particles, a thermal dewetting process was conducted at 600 °C for 5 min in the active area and 700 °C for 10 min in the edge area by using a rapid thermal annealing system (KVR-4000, Korea Vacuum Tech, Ltd., Korea) under a nitrogen environment. The thermal dewetting process occurred by the energy competition between destabilizing energy (long-range attractive forces, van der Waals interaction) and stabilizing energy (surface tension of the metal film−substrate) (see Figure S13, Supporting Information).[60] Therefore, the annealing temperature controls the morphology of dewetted particle shape/distribution. In the initial state, the annealing process promotes the formation of elongated islands; sequentially, they make it a round-shaped island. As the thickness of the film is thicker, the required temperature/time is higher to make a round-shaped island; in total, the thickness of the metal film, temperature, and annealing time determine the morphology of the dewetted surface.[35] Therefore, we applied different temperatures and times to obtain well-dispersed and rounded nano-/microparticles. Subsequently, the Ag layers were patterned by a reactive ion etch system (PLASMA LAB80, Oxford Instruments, UK) using CF$_4$ (50 sccm) at a RF power of 65 W for 10 min (active area) and 5 min (edge area). The samples were dipped into nitric acid (HNO$_3$) to remove the residual Ag at room temperature (25 °C) for 3 s. Sequentially, the reverse-shaped Ni master mold was fabricated. On the glass hybrid structure, the seed layer (i.e., Cu) was sputtered and the electroplating process is taken. After process, the back plane of Ni was planarized; then, the Ni stamp was released from the glass structure. To fabricate the HDS-PDMS layer, the PDMS was mixed with a base elastomer with a cross-linking agent ratio of 10:1 (Sylgard 184, Dow Corning, USA). The blended polymer was placed in a vacuum chamber for 30 min to eliminate the air bubbles. Subsequently, the PDMS was spin-coated on the self-assembled monolayer-coated patterned Ni mold at 500 rpm for 30 s and annealed at 60° for 12 h. The cured HDS-PDMS layer was detached from the patterned Ni mold.

PV Characterization of Solar Cells. The current density−voltage curves were plotted by using a solar simulator with AM 1.5 G (Oriel Sol3A, Newport, USA) and 1 sun illumination (100 Mw/cm^2). For accurate measurements, the light intensity was calibrated with a silicon reference cell (Oriel SRC-1000 TC KG5-N, Newport, USA).

■ ASSOCIATED CONTENT

ⓢ Supporting Information

The Supporting Information is available free of charge at https://pubs.acs.org/doi/10.1021/acsami.2c12131.

> Fabrication process, quantitative calculation, structural analysis, and schematic illustration of the detailed result of the fabricated/calculated structure (PDF)

■ AUTHOR INFORMATION

Corresponding Author

Young Min Song — *School of Electrical Engineering and Computer Science, Gwangju Institute of Science and Technology, Gwangju 61005, Republic of Korea; Artificial Intelligence (AI) Graduate School, Gwangju Institute of Science and Technology, Gwangju 61005, Korea;* ⊙ orcid.org/0000-0002-4473-6883; Email: ymsong@gist.ac.kr

Authors

Joo Hwan Ko — *School of Electrical Engineering and Computer Science, Gwangju Institute of Science and Technology, Gwangju 61005, Republic of Korea;* ⊙ orcid.org/0000-0001-8129-4319

So Hee Kim — *School of Electrical Engineering and Computer Science, Gwangju Institute of Science and Technology, Gwangju 61005, Republic of Korea*

Min Seok Kim — *School of Electrical Engineering and Computer Science, Gwangju Institute of Science and Technology, Gwangju 61005, Republic of Korea*

Se-Yeon Heo — *School of Electrical Engineering and Computer Science, Gwangju Institute of Science and Technology, Gwangju 61005, Republic of Korea*

Young Jin Yoo — *School of Electrical Engineering and Computer Science, Gwangju Institute of Science and Technology, Gwangju 61005, Republic of Korea*

Yeong Jae Kim — *Korea Institute of Ceramic Engineering and Technology, Ceramics Test-Bed Center, Icheon-si, Gyeonggi-do 17303, Republic of Korea*

Heon Lee — *Department of Materials Science and Engineering, Korea University, Seoul 02841, Republic of Korea;* ⊙ orcid.org/0000-0001-6635-1880

Complete contact information is available at:
https://pubs.acs.org/10.1021/acsami.2c12131

Author Contributions

J.H.K. and S.H.K. contributed equally to this work. Y.M.S. conceived and supervised the project. J.H.K and S.H.K. conducted the theoretical and simulation works. J.H.K., S.H.K., and Y.J.Y. designed and performed the experiments. J.H.K., S.H.K., M.S.K., and S.-Y.H. measured and characterized the experimental results. J.H.K. and S.H.K. drafted the manuscript. Y.J.K., H.L., and Y.M.S. reviewed and edited the manuscript. All authors have given approval to the final version of the manuscript.

Notes

The authors declare no competing financial interest.

■ REFERENCES

(1) Trube, J.; Fischer, M.; Erfert, G.; Li, C.; Ni, P.; Woodhouse, M.; Li, P.; Metz, A.; Saha, I.; Chen, R. *International Technology Roadmap for Photovoltaic (ITRPV)*; VDMA photovoltaic equipment, 2018; Vol. 24, pp 77−97.

(2) Peters, I. M.; Rodriguez Gallegos, C. D. R.; Sofia, S. E.; Buonassisi, T. The Value of Efficiency in Photovoltaics. *Joule* **2019**, *3*, 2732−2747.

(3) Garnett, E. C.; Ehrler, B.; Polman, A.; Alarcon-Llado, E. Photonics for Photovoltaics: Advances and Opportunities. *ACS Photonics* **2020**, *8*, 61−70.

(4) Xu, C. Y.; Hu, W.; Wang, G.; Niu, L.; Elseman, A. M.; Liao, L.; Yao, Y.; Xu, G.; Luo, L.; Liu, D.; Zhou, G.; Li, P.; Song, Q. Coordinated Optical Matching of a Texture Interface Made from Demixing Blended Polymers for High-Performance Inverted Perovskite Solar Cells. *ACS Nano* **2019**, *14*, 196−203.

(5) Zhang, H.; Toudert, J. Optical Management for Efficiency Enhancement in Hybrid Organic-Inorganic Lead Halide Perovskite Solar Cells. *Sci. Technol. Adv. Mater.* **2018**, *19*, 411−424.

(6) van Eerden, M.; Jaysankar, M.; Hadipour, A.; Merckx, T.; Schermer, J. J.; Aernouts, T.; Poortmans, J.; Paetzold, U. W. Optical Analysis of Planar Multicrystalline Perovskite Solar Cells. *Adv. Opt. Mater.* **2017**, *5*, 1700151.

(7) Yang, Y.; Yan, Y.; Yang, M.; Choi, S.; Zhu, K.; Luther, J. M.; Beard, M. C. Low Surface Recombination Velocity in Solution-Grown CH3NH3PbBr3 Perovskite Single Crystal. *Nat. Commun.* **2015**, *6*, 7961.

(8) Khoram, P.; Oener, S. Z.; Zhang, Q.; Fan, Z.; Garnett, E. C. Surface Recombination Velocity of Methylammonium Lead Bromide Nanowires in Anodic Aluminium Oxide Templates. *Mol. Syst. Des. Eng.* **2018**, *3*, 723−728.

(9) Chen, F.-h.; Pathreeker, S.; Kaur, J.; Hosein, I. D. Increasing Light Capture in Silicon Solar Cells with Encapsulants Incorporating Air Prisms to Reduce Metallic Contact Losses. *Opt. Express* **2016**, *24*, A1419−A1430.

(10) Schumann, M. F.; Fritz, B.; Eckstein, R.; Lemmer, U.; Gomard, G.; Wegener, M. Cloaking of Metal Grid Electrodes on Lambertian Emitters by Free-form Refractive Surfaces. *Opt. Lett.* **2018**, *43*, 527−530.

(11) Lee, J.; Moon, Y. J.; Cho, J.; Park, S.; Baek, S.; Nam, M.; Kim, S. K.; Ko, D. H. Hierarchically Designed Light Trapping Films for All-Day Operating Semitransparent Photovoltaics. *Adv. Energy Mater.* **2020**, *10*, 2001450.

(12) Biria, S.; Chen, F. H.; Pathreeker, S.; Hosein, I. D. Polymer Encapsulants Incorporating Light-Guiding Architectures to Increase Optical Energy Conversion in Solar Cells. *Adv. Mater.* **2018**, *30*, 1705382.

(13) Wang, D.-L.; Cui, H.-J.; Hou, G.-J.; Zhu, Z.-G.; Yan, Q.-B.; Su, G. Highly Efficient Light Management for Perovskite Solar Cells. *Sci. Rep.* **2016**, *6*, 18922.

(14) Hwang, I.; Choi, D.; Lee, S.; Seo, J. H.; Kim, K.-H.; Yoon, I.; Seo, K. Enhancement of Light Absorption in Photovoltaic Devices Using Textured Polydimethylsiloxane Stickers. *ACS Appl. Mater. Interfaces* **2017**, *9*, 21276−21282.

(15) Hwang, I.; Jeong, Y.; Shiratori, Y.; Park, J.; Miyajima, S.; Yoon, I.; Seo, K. Effective Photon Management of Non-Surface-Textured Flexible Thin Crystalline Silicon Solar Cells. *Cell Rep. Phys. Sci.* **2020**, *1*, 100242.

(16) Tavakoli, M. M.; Tsui, K.-H.; Zhang, Q.; He, J.; Yao, Y.; Li, D.; Fan, Z. Highly Efficient Flexible Perovskite Solar Cells with Antireflection and Self-Cleaning Nanostructures. *ACS Nano* **2015**, *9*, 10287−10295.

(17) Jeong, S.; Garnett, E. C.; Wang, S.; Yu, Z.; Fan, S.; Brongersma, M. L.; McGehee, M. D.; Cui, Y. Hybrid Silicon Nanocone-Polymer Solar Cells. *Nano Lett.* **2012**, *12*, 2971−2976.

(18) Wang, Y.; Wang, P.; Zhou, X.; Li, C.; Li, H.; Hu, X.; Li, F.; Liu, X.; Li, M.; Song, Y. Diffraction-Grated Perovskite Induced Highly Efficient Solar Cells through Nanophotonic Light Trapping. *Adv. Energy Mater.* **2018**, *8*, 1702960.

(19) Deng, K.; Liu, Z.; Wang, M.; Li, L. Nanoimprinted Grating-Embedded Perovskite Solar Cells with Improved Light Management. *Adv. Funct. Mater.* **2019**, *29*, 1900830.

(20) Gensch, M.; Schwartzkopf, M.; Ohm, W.; Brett, C. J.; Pandit, P.; Vayalil, S. K.; Bießmann, L.; Kreuzer, L. P.; Drewes, J.; Polonskyi, O.; Strunskus, T.; Faupel, F.; Stierle, A.; Müller-Buschbaum, P.; Roth, S. V. Correlating Nanostructure, Optical and Electronic Properties of Nanogranular Silver Layers During Polymer-Template-Assisted Sputter Deposition. *ACS Appl. Mater. Interfaces* **2019**, *11*, 29416−29426.

(21) Pala, R. A.; Liu, J. S.; Barnard, E. S.; Askarov, D.; Garnett, E. C.; Fan, S.; Brongersma, M. L. Optimization of Non-Periodic Plasmonic Light-Trapping Layers for Thin-Film Solar Cells. *Nat. Commun.* **2013**, *4*, 2095.

(22) Li, Z.; Ma, T.; Li, S.; Gu, W.; Lu, L.; Yang, H.; Dai, Y.; Wang, R. High-Efficiency, Mass-Producible, and Colored Solar Photovoltaics Enabled by Self-Assembled Photonic Glass. *ACS Nano* **2022**, *16*, 11473.

(23) Yoo, Y. J.; Kim, Y. J.; Kim, S.-Y.; Lee, J. H.; Kim, K.; Ko, J. H.; Lee, J. W.; Lee, B. H.; Song, Y. M. Mechanically Robust Antireflective Moth-Eye Structures with a Tailored Coating of Dielectric Materials. *Opt. Mater. Express* **2019**, *9*, 4178−4186.

(24) Lee, W.; Yoo, Y. J.; Park, J.; Ko, J. H.; Kim, Y. J.; Yun, H.; Kim, D. H.; Song, Y. M.; Kim, D.-H. Perovskite Microcells Fabricated Using Swelling-Induced Crack Propagation for Colored Solar Windows. *Nat. Commun.* **2022**, *13*, 1946.

(25) Kim, Y. J.; Yoo, Y. J.; Yoo, D. E.; Lee, D. W.; Kim, M. S.; Jang, H. J.; Kim, Y.-C.; Jang, J.-H.; Kang, I. S.; Song, Y. M. Enhanced Light Harvesting In Photovoltaic Devices Using an Edge-Located One-Dimensional Grating Polydimethylsiloxane Membrane. *ACS Appl. Mater. Interfaces* **2019**, *11*, 36020−36026.

(26) Cho, E.; Kim, Y. Y.; Ham, D. S.; Lee, J. H.; Park, J.-S.; Seo, J.; Lee, S.-J. Highly Efficient and Stable Flexible Perovskite Solar Cells Enabled by Using Plasma-Polymerized-Fluorocarbon Antireflection Layer. *Nano Energy* **2021**, *82*, 105737.

(27) Juan, F.; Wu, Y.; Shi, B.; Wang, M.; Wang, M.; Xu, F.; Jia, J.; Wei, H.; Yang, T.; Cao, B. Plasmonic Au Nanooctahedrons Enhance Light Harvesting and Photocarrier Extraction in Perovskite Solar Cell. *ACS Appl. Energy Mater.* **2021**, *4*, 3201−3209.

(28) Kelzenberg, M. D.; Boettcher, S. W.; Petykiewicz, J. A.; Turner-Evans, D. B.; Putnam, M. C.; Warren, E. L.; Spurgeon, J. M.; Briggs, R. M.; Lewis, N. S.; Atwater, H. A. Enhanced Absorption And Carrier Collection in Si Wire Arrays for Photovoltaic Applications. *Nat. Mater.* **2010**, *9*, 239−244.

(29) In, S.; Mason, D. R.; Lee, H.; Jung, M.; Lee, C.; Park, N. Enhanced Light Trapping and Power Conversion Efficiency in Ultrathin Plasmonic Organic Solar Cells: A Coupled Optical-Electrical Multiphysics Study on the Effect of Nanoparticle Geometry. *ACS Photonics* **2015**, *2*, 78−85.

(30) Peer, A.; Biswas, R. Nanophotonic Organic Solar Cell Architecture for Advanced Light Trapping with Dual Photonic Crystals. *ACS Photonics* **2014**, *1*, 840−847.

(31) Wei, J.; Xu, R. P.; Li, Y. Q.; Li, C.; Chen, J. D.; Zhao, X. D.; Xie, Z. Z.; Lee, C. S.; Zhang, W. J.; Tang, J. X. Enhanced Light Harvesting in Perovskite Solar Cells by a Bioinspired Nanostructured Back Electrode. *Adv. Energy Mater.* **2017**, *7*, 1700492.

(32) Neder, V.; Luxembourg, S. L.; Polman, A. Efficient Colored Silicon Solar Modules Using Integrated Resonant Dielectric Nano-scatterers. *Appl. Phys. Lett.* **2017**, *111*, 073902.

(33) Li, K.; Zhang, Y.; Zhen, H.; Wang, H.; Liu, S.; Yan, F.; Zheng, Z. Versatile Biomimetic Haze Films for Efficiency Enhancement of Photovoltaic Devices. *J. Mater. Chem. A* **2017**, *5*, 969−974.

(34) Chang, T.-W.; Gartia, M. R.; Seo, S.; Hsiao, A.; Liu, G. L. A Wafer-Scale Backplane-Assisted Resonating Nanoantenna Array SERS Device Created by Tunable Thermal Dewetting Nanofabrication. *Nanotechnology* **2014**, *25*, 145304.

(35) Serrano, A.; Llorca-Hernando, O.; del Campo, A.; Rubio-Marcos, F.; Rodríguez de la Fuente, O.; Fernández, J.; García, M. Ag-AgO Nanostructures on Glass Substrates by Solid-State Dewetting: From Extended to Localized Surface Plasmons. *J. Appl. Phys.* **2018**, *124*, 133103.

(36) Thompson, C. V. Solid-State Dewetting of Thin Films. *Annu. Rev. Mater. Res.* **2012**, *42*, 399−434.

(37) Atwater, H. A.; Polman, A. Plasmonics for Improved Photovoltaic Devices. *Nat. Mater.* **2010**, *9*, 205−213.

(38) Xia, Y.; Whitesides, G. M. Soft Lithography. *Angew. Chem., Int. Ed.* **1998**, *37*, 550−575.

(39) Song, Y. M.; Choi, H. J.; Yu, J. S.; Lee, Y. T. Design of Highly Transparent Glasses with Broadband Antireflective Subwavelength Structures. *Opt. Express* **2010**, *18*, 13063−13071.

(40) Park, G. C.; Song, Y. M.; Ha, J.-H.; Lee, Y. T. Broadband Antireflective Glasses with Subwavelength Structures using Randomly Distributed Ag Nanoparticles. *J. Nanosci. Nanotechnol.* **2011**, *11*, 6152−6156.

(41) Nam, W. I.; Yoo, Y. J.; Song, Y. M. Geometrical Shape Design of Nanophotonic Surfaces for Thin Film Solar Cells. *Opt. Express* **2016**, *24*, A1033−A1044.

(42) Leem, J. W.; Kim, S.; Lee, S. H.; Rogers, J. A.; Kim, E.; Yu, J. S. Efficiency Enhancement of Organic Solar Cells Using Hydrophobic Antireflective Inverted Moth-Eye Nanopatterned PDMS Films. *Adv. Energy Mater.* **2014**, *4*, 1301315.

(43) Leem, J. W.; Yu, J. S. Artificial inverted compound eye structured polymer films with light-harvesting and self-cleaning functions for encapsulated III-V solar cell applications. *RSC Adv.* **2015**, *5*, 60804−60813.

(44) Yeo, C.; Kim, J. B.; Song, Y. M.; Lee, Y. T. Antireflective Silicon Nanostructures with Hydrophobicity by Metal-Assisted Chemical Etching for Solar Cell Applications. *Nanoscale Res. Lett.* **2013**, *8*, 159.

(45) Leem, J.; Song, Y.; Lee, Y.; Yu, J. Effect of Etching Parameters on Antireflection Properties of Si Subwavelength Grating Structures for Solar Cell Applications. *Appl. Phys. B: Lasers Opt.* **2010**, *100*, 891−896.

(46) Raut, H. K.; Ganesh, V. A.; Nair, A. S.; Ramakrishna, S. Anti-Reflective Coatings: A Critical, in-Depth Review. *Energy Environ. Sci.* **2011**, *4*, 3779−3804.

(47) Kim, D. H.; Dudem, B.; Jung, J. W.; Yu, J. S. Boosting Light Harvesting in Perovskite Solar Cells by Biomimetic Inverted Hemispherical Architectured Polymer Layer with High Haze Factor as an Antireflective Layer. *ACS Appl. Mater. Interfaces* **2018**, *10*, 13113−13123.

(48) Ham, J.; Dong, W. J.; Jung, G. H.; Lee, J.-L. Wavelength-Scale Structures as Extremely High Haze Films for Efficient Polymer Solar Cells. *ACS Appl. Mater. Interfaces* **2016**, *8*, 5990−5997.

(49) Kesornkhup, S.; Tuantranont, A.; Lomas, T.; Sriprachuabwong, C.; Wasapinyokul, K. Accuracy of Swanepoel Method in Calculation of Polymer Film Thicknesses. *Acta Phys. Pol.* **2021**, *140*, 113.

(50) Gulomov, J.; Aliev, R.; Mirzaalimov, A.; Mirzaalimov, N.; Kakhkhorov, J.; Rashidov, B.; Temirov, S. Studying the Effect of Light Incidence Angle on Photoelectric Parameters of Solar Cells by Simulation. *Int. J. Renewable Energy Dev.* **2021**, *10*, 731−736.

(51) Huang, Z.; Cheng, L.; Wu, B.; Wu, X. The Study of Optical and Electrical Properties of Solar Cells with Oblique Incidence. *IEEE Photonics Technol. Lett.* **2016**, *28*, 2047−2049.

(52) Rahman, M. M. Polyurethane/Zinc Oxide (PU/ZnO) Composite-Synthesis, Protective Property and Application. *Polymers* **2020**, *12*, 1535.

(53) Hang, T. T. X.; Dung, N. T.; Truc, T. A.; Duong, N. T.; Van Truoc, B.; Vu, P. G.; Hoang, T.; Thanh, D. T. M.; Olivier, M.-G. Effect of Silane Modified Nano ZnO on UV Degradation of Polyurethane Coatings. *Prog. Org. Coat.* **2015**, *79*, 68−74.

(54) Fan, Z.; Kapadia, R.; Leu, P. W.; Zhang, X.; Chueh, Y.-L.; Takei, K.; Yu, K.; Jamshidi, A.; Rathore, A. A.; Ruebusch, D. J.; Wu, M.; Javey, A. Ordered Arrays of Dual-Diameter Nanopillars for Maximized Optical Absorption. *Nano Lett.* **2010**, *10*, 3823−3827.

(55) Wang, H.-P.; Lin, T.-Y.; Tsai, M.-L.; Tu, W.-C.; Huang, M.-Y.; Liu, C.-W.; Chueh, Y.-L.; He, J.-H. Toward Efficient and Omnidirectional N-type Si Solar Cells: Concurrent Improvement in Optical and

Electrical Characteristics by Employing Microscale Hierarchical Structures. *ACS Nano* **2014**, *8*, 2959−2969.

(56) Al-Maawali, S.; Bemis, J. E.; Akhremitchev, B. B.; Leecharoen, R.; Janesko, B. G.; Walker, G. C. Study of the Polydispersity of Grafted Poly(dimethylsiloxane) Surfaces Using Single-Molecule Atomic Force Microscopy. *J. Phys. Chem. B* **2001**, *105*, 3965−3971.

(57) Amotchkina, T.; Trubetskov, M.; Hahner, D.; Pervak, V. Characterization of e-beam evaporated Ge, YbF3, ZnS, and LaF3 thin films for laser-oriented coatings. *Appl. Opt.* **2020**, *59*, A40−A47.

(58) Rakić, A. D.; Majewski, M. L. Modeling the Optical Dielectric Function of GaAs and AlAs: Extension of Adachi's Model. *J. Appl. Phys.* **1996**, *80*, 5909−5914.

(59) Adachi, S. Optical dispersion relations for GaP, GaAs, GaSb, InP, InAs, InSb, AlxGa1−xAs, and In1−xGaxAsyP1−y. *J. Appl. Phys.* **1989**, *66*, 6030−6040.

(60) Owusu-Ansah, E.; Birss, V. I.; Shi, Y. Mechanisms of Pulsed Laser-Induced Dewetting of Thin Platinum Films on Tantalum Substrates-A Quantitative Study. *J. Phys. Chem. C* **2020**, *124*, 23387−23393.